Plasma evolution from laser-driven gold disks. I. Experiments and results

E. F. Gabl
Department of Physics, Eastern Michigan University, Ypsilanti, Michigan 48197 and KMS Fusion Inc., Ann Arbor, Michigan 48106

B. H. Failor and Gar. E. Busch
KMS Fusion Inc., Ann Arbor, Michigan 48106

R. J. Schroeder
Schlumberger-Doll Research, 1 Quarry Road, Ridgefield, Connecticut 06887 and KMS Fusion Inc., Ann Arbor, Michigan 48106

D. Ress and L. Suter
Lawrence Livermore National Laboratory, Livermore, California 94550

(Received 13 March 1990; accepted 11 June 1990)

Gold disk targets were irradiated with green ($\lambda = 0.53\ \mu$m) laser light at intensities between 0.5 and 5×10^{14} W/cm^2 using shaped laser pulses. Plasma conditions near and below critical density ($n_c \simeq 4\times10^{21}$/cm^3) were determined from three diagnostics. Streaked one-dimensional images of the M-band emission (2–3.5 keV) along the laser axis yield the peak emission trajectory. Temporally and spatially averaged measurements of the hard x-ray spectrum (4–25 keV) were used to determine the average coronal electron temperature. Holographic interferometry was used to determine the electron density profiles and scale lengths along the laser axis. The peak emission trajectory, electron temperature, and scale lengths are all in good agreement with simulations, but the magnitudes of the electron density profiles are not, as discussed in an accompanying paper [Phys. Fluids B 2, 2448 (1990)].

I. INTRODUCTION

Knowledge of the behavior of bulk plasma from laser-irradiated high-Z materials is critical to the design of radiatively driven targets. In particular, the plasma temperature and density profile not only affect the radiation field, but also laser energy deposition and hot electron production from parametric instabilities such as stimulated Raman scattering (SRS), stimulated Brillouin scattering (SBS), and filamentation. To improve our understanding of the dynamics of the laser-irradiated coronal plasma from gold disk targets, we have performed both experiments (described in this paper), and simulations[1] using the hydrocode LASNEX[2] (described in the following paper, referred to as II). Several experiments have been carried out prior to this one on both disk and spherical targets and short wavelengths. These experiments have emphasized hot electron production and parametric instabilities,[3-7] conversion efficiency of laser light to x rays,[8-14] and energy transport.[15] In contrast, the experiments to be discussed here emphasize characterization of the plasma (temperature and density) near and below critical density ($n_c \simeq 4\times10^{21}$/cm^3) as a function of irradiation parameters of interest to indirect drive fusion. The laser pulse shape (850 psec and 2 nsec square, and picket pulse trains) and intensity ($I = 0.5$–5×10^{14} W/cm^2) are similar to those used on the NOVA[16] laser for indirect drive experiments.

The coronal plasma density profile from densities of 2×10^{19}/cm^3 to about 4×10^{20}/cm^3 ($n_c/200$ to $n_c/10$) was determined by holographic interferometry. Since parametric processes occur only if the plasma density scale length, defined by $L = n_e(dn_e/dx)^{-1}$, exceeds a threshold, we discuss the temporal evolution of the scale length as well as the plasma density profiles. Hydrocode simulations show that peak gold M-band emission (2–3.5 keV) should be observed between $n_c/2$ and $n_c/4$. Therefore, we use the peak M-band emission to indicate the approximate trajectory of the higher density plasma that cannot be probed optically. The space- and time-averaged coronal temperature was determined by fitting the x-ray recombination emission spectrum to an exponential (assuming Maxwellian electrons).

We summarize our results as follows.

(i) Absorption was from 75% to 90% of the incident laser energy for all of the pulse shapes, increasing with decreasing average laser intensity. This is in good agreement with previous experiments using square or Gaussian-shaped laser pulses.[3-15]

(ii) The measured average coronal temperatures were from 1.5 to 2.4 keV. This is in good agreement with nonflux-limited simulations (see II) and scaling laws from previous LASNEX simulations.[6]

(iii) The measured plasma density scale lengths were from 100 to 200 μm in the $n_c/10$ to $n_c/40$ region. Although the coronal density profiles from the simulations overestimate the plasma density, the scale lengths match very well.

(iv) The peak M-band emission (along the laser axis) occurred up to 100 μm from the target surface, with an instantaneous velocity dependent on the pulse shape. The measured velocity was 3–7×10^6 cm/sec.

(v) A retrograde motion of the peak M-band emission was observed for the picket pulse train shapes. This is predicted by the simulations, and may be due to profile steepening.

(vi) Jetting of the plasma was observed for the picket pulse train shapes. We observe that relatively cold, dense plasma jets arise from cold spots in the laser intensity pattern.

 0899-8221/90/102437-11$02.00

This paper is organized as follows. Section II contains a description of the experimental parameters, that is, the laser, targets, diagnostics, and experimental procedures. Data are presented and discussed in Sec. III. Section IV contains the summary. The results of these experiments are compared in detail in II to one-dimensional hydrocode simulations.

II. EXPERIMENTAL ARRANGEMENTS

The parameters varied in the experiment were laser pulse shape, intensity, and spot size (Sec. II A). The targets and alignments are discussed in Sec. II B. The primary x-ray measurements were spatially resolved (along the laser axis) and streaked gold M-band emission and high energy (5–20 keV) x-ray flux (Sec. II C). Optical probing (Sec. II D) was used to obtain holographic interferograms.

A. Laser configuration

The Chroma[17] laser at KMS was used for the experiment. A mode-locked YLF oscillator produced a Gaussian laser pulse of 120 ± 10 psec full width half-maximum (FWHM). Pulse shaping was achieved by splitting this pulse into 13 individual pulses spaced by 170 psec. The amplitude of each of the individual pulses was varied by apertures. The pulses were then recombined to form a continuous pulse of up to 2 nsec duration. The resulting laser pulse was then amplified to produce an energy of up to 400 J and then frequency doubled (2ω) to 0.5265 μm using a KDP type II crystal. The conversion efficiency to harmonic light was about 50% yielding up to 200 J of energy on target. Several different pulse shapes were used. Square pulses were formed using six 120 psec pulses to obtain a pulse of about 850 psec FWHM [Fig. 1(a)]. Three types of longer pulses were used. Two nanosecond square pulses used all thirteen 120 psec pulses with equal amplitude [Fig. 1(b)]. Pickets + square pulses [Fig. 1(c)] were formed by using pulses 1 (the first picket), 6 (the second picket), and 8 through 13 (the square portion). The maximum powers of the pulses were in the ratio 1:2:3, so most of the energy (typically 100–125 J) was in the square portion of the pulse. Additionally, several target experiments were done using only the first two pickets. Pulses with monotonically increasing power [t-squared, see Fig. 1(d)] were used. We note that for any of the pulse shapes, there were fluctuations in the power levels of up to 30% in addition to variations in the energy and overall pulse length. Therefore, the pulse lengths quoted above are nominal.

The pulse shapes were measured using a Hamamatsu optical streak camera with an S20 photocathode. The temporal resolution was 5 psec. The streak camera sampled either a 2 cm portion of the beam, or the whole beam, using leakage through a turning mirror. The incident power was obtained by normalizing the streak camera signal to the energy incident on target as measured with a calorimeter. The peak intensities quoted later in this paper are calculated using the FWHM of the laser spot assuming a Gaussian spatial profile.

The focusing optic was an $f/6$ aspheric lens. For the majority of the irradiations the target was placed either 1200 or 3000 μm on the divergent side of best focus. The spot size was either 200 or 500 μm, giving nominal peak intensities $0.5\text{–}5 \times 10^{14}$ W/cm^2. Several experiments had the target placed on the convergent side of best focus to generate a particularly nonuniform spatial intensity distribution.

A portion of the incident laser was split off to a far-field imaging system to record the time integrated intensity pattern. The images were recorded using either film or a CCD camera with a frame grabbing system. When using film, an etalon provided a series of images which could be used to generate a density versus log of exposure curve to linearize the film. An example of a line out of the intensity pattern is shown in Fig. 2 for a 1200 μm offset from best focus. On the

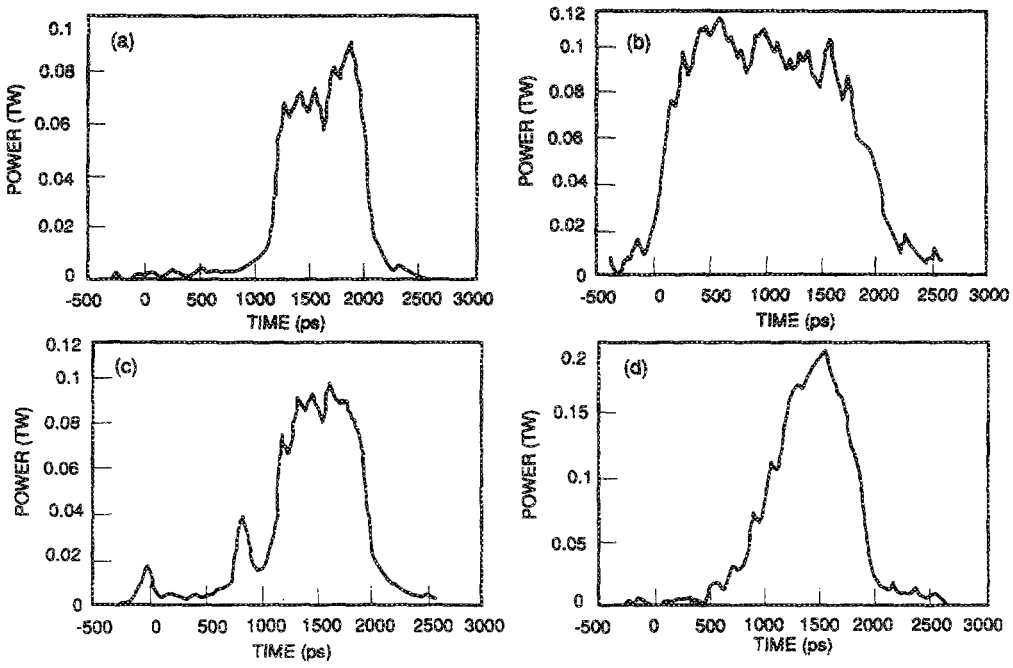

FIG. 1. Various laser pulse shapes were used to irradiate the targets. The rise time was about 50 psec for each pulse shape. Square pulses (a) were 850 psec FWHM. Longer pulses were also used, including 2 nsec square (b), pickets + square (c), and t-squared (d) shapes.

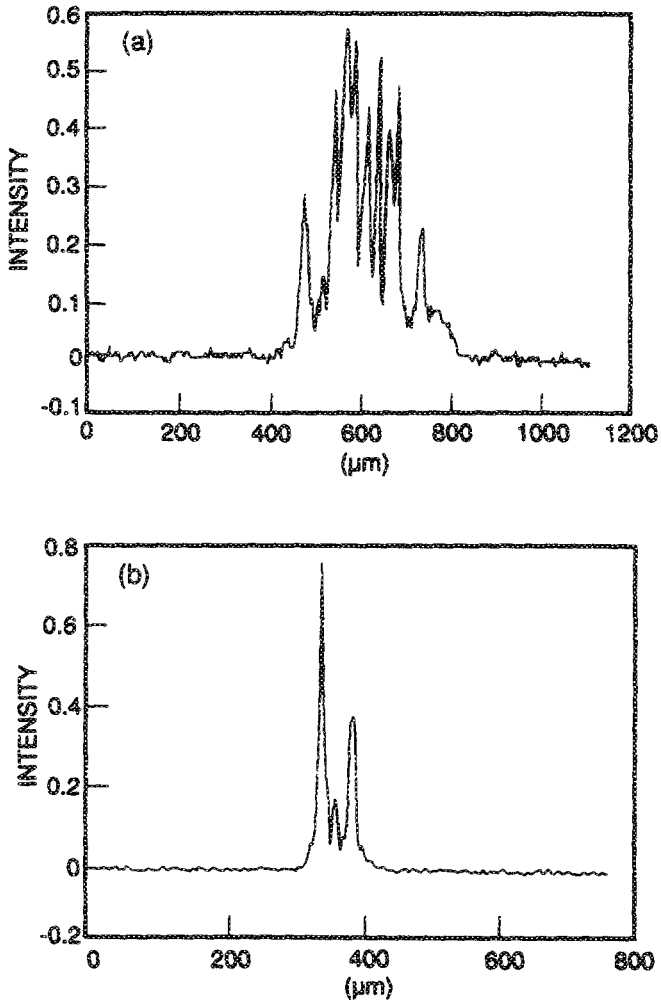

FIG. 2. Lineouts of the time integrated laser intensity pattern for a 1200 μm focal offset show the irregularities of the beam. The divergent side of focus (a) shows a spikey intensity pattern modulating a Gaussian envelope. The convergent side of focus (b) shows a spikey pattern superimposed on a hot ring.

divergent side of best focus [Fig. 2(a)], there is a random distribution of high intensity "hot" spots, which arise from scattering and self-focusing in the laser amplifiers. The width of these regions is 20–50 μm separated by 30–40 μm with peak to valley variations of factors of 2–4. Between 80% and 90% of the laser energy is within the 200 μm spot. On the convergent side of best focus [Fig. 2(b)] we find a high-intensity hot ring, 10 μm FWHM at a radius of 40 μm. The ring is caused by spherical aberration in the laser system. The intensity of the peak of the ring is about 3–8 times that in the center of the spot. Between 50% and 60% of the laser energy is within the 200 μm spot.

The characteristics of the laser spot patterns were similar for the 3000 μm offset. On the divergent side of focus were 20 μm wide spikes spaced 20–40 μm apart with factors of 2 to 4 intensity variation. The 85% energy diameter was 500 μm. On the convergent side, the hot ring was 20 μm thick and was elliptically shaped, 140 μm across on the short side, 250 μm on the long side. The peak intensity was about five times higher in the ring as compared to the average in the center. Ninety percent of the energy was within a 300 μm diameter.

B. Targets and alignment

The majority of targets were gold disks 22 μm thick and 600 μm in diameter. Each disk was glued near the end of a 25–50 μm thick, 3 mm long glass fiber. (Additionally, CH, Al, and Ag targets of similar dimensions were used in similar experiments for Z scaling comparisons.) The targets were aligned along the laser axis by first finding best focus using the reflection of a continuous-wave argon laser. The target was then offset to the distances stated in the previous section, taking the wavelength difference between the alignment and main lasers into account. All alignments occurred from 5 to 10 min prior to the target irradiation. X-ray pinhole images and interferograms indicate that most target alignments had the center of the beam within 50 μm of the center of the target.

C. X-ray diagnostics

The experimental setup is shown in Fig. 3. Pinhole cameras were used to obtain time integrated images of the emission both parallel and perpendicular to the target surface. Each pinhole camera had an array of four pinholes, 5–10 μm in diameter spaced 500 μm apart. The pinhole array was placed about 1 cm from the target and the x-ray film was placed about 10 cm from the pinhole array, giving a magnification of about 10. Since the spacing between pinholes was known, the magnification could be calculated precisely from the image spacing. Different filters were used for each pinhole to increase the effective dynamic range. Typical filtering was 25 μm of beryllium and 3–7 μm of tin (peak L edge transmission of 3.8 keV). The images were recorded on Kodak direct exposure film. The product of the filter and the theoretical film x-ray response functions shows that the peak sensitivity is within the gold M-band spectrum.

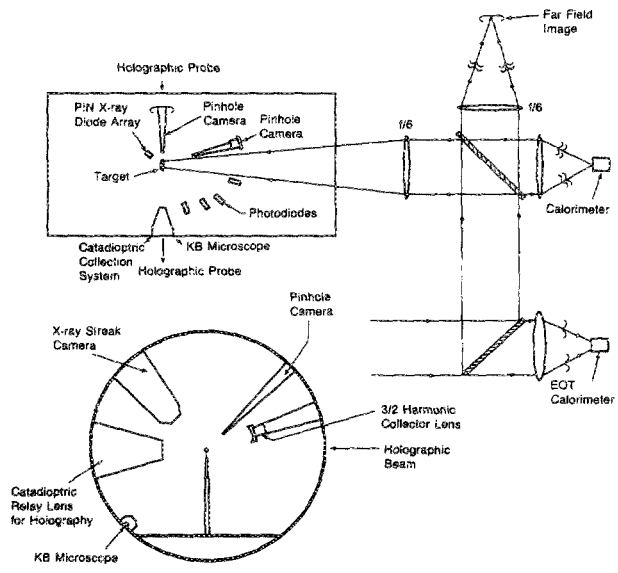

FIG. 3. The experimental setup consisted of optical and x-ray diagnostics placed about the target. The major instruments have a line of sight orthogonal to the incident laser beam.

A Kirkpatrick–Baez[18] microscope was used to obtain both hard (1–2 keV) and soft (600–800 eV) time integrated images of the emission parallel to the target surface. The microscope consists of four pairs of cylindrical quartz mirrors. Two pairs are coated with gold, and two pairs are uncoated. The angle of incidence is about 1.7°. The gold mirrors are sensitive up to 2 keV, and the quartz mirrors are sensitive to 1 keV for this angle of incidence. The filtering for the gold and quartz channels were, respectively, 25–50 μm of beryllium and 0.6 μm of nickel. The images were recorded on Kodak direct exposure film. Images from the higher energy gold channels were in good qualitative agreement with those obtained from the pinhole camera. The microscope was designed for a magnification of 3 with the mirrors placed 30 cm from the target and the image plane 90 cm from the mirrors. For each channel, four images are obtained—a direct shine through image, a one-dimensional image from each mirror, and the two-dimensional image from the reflection off of both mirrors. Normally, a spatial filter removes all but the two-dimensional image. However, a misalignment of the mirrors caused a second image from a single reflection to appear behind the target image for the soft x-ray channels. This did not interfere with the data in the region of interest. A wire grid (25 μm center to center spacing, 7 μm wires) placed at the target was used to obtain resolution images. From this and other similar data, we determine that the resolution was better than 25 μm.

One-dimensional streak images of the gold M-band emission perpendicular to the target surface were obtained using a Kentech x-ray streak camera. A 15 μm slit was used to image the emission onto a second slit (width = 100 μm) placed in front of the streak camera photocathode. The camera sweep speed (67 psec/mm) has been calibrated in a separate experiment using a sequence of x rays generated by laser pulses of known temporal spacing. The spatial and temporal resolutions of the x-ray streaks were, respectively, about 15 μm and 7 psec. The imaging slit filter was 25 μm of beryllium and 3–7 μm of tin. The photocathode consisted of 300 Å of gold deposited on a 0.2 μm Formvar substrate. The overall (filter + photocathode) sensitivity for the slit imaging was primarily in the M-band region (2–3.5 keV). Neither a temporal nor a spatial fiducial was available for the streak camera. We therefore assume in our analysis that the initial x-ray emission occurs near the initial target surface. This is supported by time-integrated pinhole images taken orthogonal to the laser direction, and showing a well-defined edge to the emission region that we take to be the target surface. The temporal origin of the emission can be determined to within 50 psec by correlating the x-ray emission maxima with the maxima of the laser pulse.

The coronal electron temperature (T_e) was estimated by fitting x-ray data in the range of 4 to 25 keV to an exponential distribution. The x rays were detected with four PIN diodes (Table I), filtered to minimize the contribution from the M band (2–4 keV) and the L band (9–11 keV). The diode sensitivity and filter response were multiplied to form an overall detector response. The diode outputs were measured by charge integrators. The diodes were placed slightly behind the target so as to obscure the first 100 μm in front of the target as described in II. The estimated temperatures represent a temporal and spatial average for the coronal plasma.

TABLE I. The filters, peak response, and bandwidth (FWHM) are listed for the diodes used to measure hard x-ray flux. The data are fit to an x-ray spectrum which assumes a Maxwellian electron distribution to obtain an estimate of the average coronal electron temperature.

Diode filter	Peak response energy (keV)	Bandwidth (keV)
Ti	5,20	1,15
Cu	8	2
Y	17	4
Ag	25	6

The M-band emission was measured by PIN diodes at various angles around the target. The diodes were filtered by 25 μm of beryllium and 3–7 μm of tin. The filtered diode response functions were multiplied by a nominal M-band x-ray spectrum to obtain an estimate of the total M-band x-ray fluence. The total energy was calculated by a nonlinear fit to the angular data assuming cylindrical symmetry with respect to the laser axis.

D. Optical diagnostics

Holographic interferometry was used to measure the electron density.[19] A pulse from the master Chroma oscillator is shortened to about 20 psec by a regenerative oscillator, frequency quadrupled to 0.263 μm, and split into 16 pulses. Each interferogram is made by overlaying holograms taken before and during the irradiation of the target. The spatial resolution of the system is better than 5 μm. Up to four interferograms (referred to as frames) spaced by 400 psec were taken for each experiment. The time of the first frame was varied with respect to the peak of the first 120 psec pulse from the oscillator. A digitized interferogram for a square laser pulse is shown in Fig. 4. Assuming azimuthal symmetry about the laser axis, we Abel invert the digitized fringes to obtain an estimate of the electron density profile. Fringes could be observed corresponding to densities as high as $8\times10^{20}/\text{cm}^3$ at early times in the laser irradiation when path lengths through the plasma are short, but profiles were generally limited to a peak electron density $n_e \leqslant 4\times10^{20}/\text{cm}^2$.

The $3/2\omega$ harmonic light generated by scattering laser light from plasmons created by two plasmon decay was used to monitor the quarter critical surface. The light was collected by an $f/22$ parabolic mirror of focal length 15 cm placed inside the target chamber. The light was relayed out of the target chamber and imaged with an $f/2$ parabola of focal length 110 cm. The overall magnification of the system was about 7. The light was filtered by a 20 nm FWHM, 3-cavity bandpass filter and various neutral density filters. The resultant image was placed on the slit of a streak camera to obtain a one-dimensional temporally resolved image of the quarter critical surface. The overall spatial resolution of the system was better than 10 μm and the temporal resolution was better than 10 psec. The data obtained by this system were in good qualitative agreement with the data obtained from the

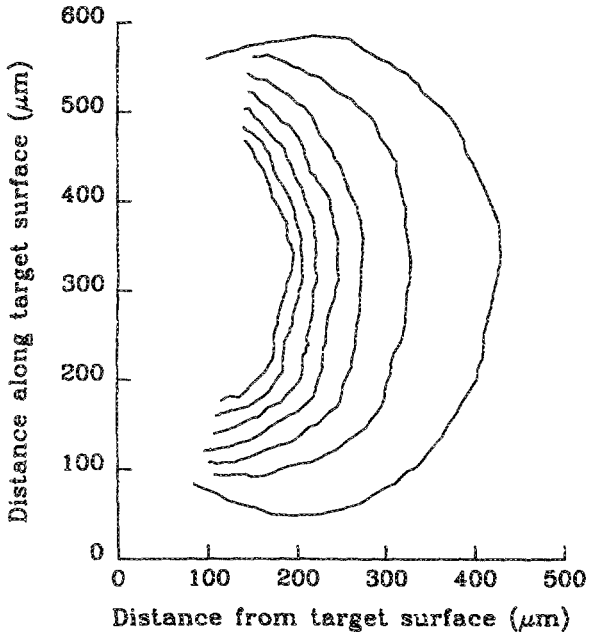

FIG. 4. A typical digitized interferogram for a square laser pulse shows nearly symmetrical fringes that can be Abel inverted to yield plasma density.

M-band x-ray streaks. Since refraction and rescattering of the $3/2\omega$ light can cause some uncertainty as to its spatial origin, we will limit our future discussions of the 0.25 to 0.5 critical density trajectory to that obtained by the x-ray streak imaging.

The scattered laser energy was measured in two ways. That portion of the laser energy scattered back into the focusing lens was collected from leakage through a turning mirror. This light was refocused onto a calorimeter using a second lens. The light scattered into the focusing lens typically accounted for 20%–30% of the total scattered laser energy. An array of filtered PIN diodes was placed in the horizontal plane around the target at increments of about 15° to collect the light scattered outside the focusing lens. The calorimeter and PIN diode signals were fit to an exponential distribution in the polar angle. Integration of this distribution gives the total scattered energy (assuming azimuthal symmetry) and thus the absorbed energy fraction.

III. EXPERIMENTAL RESULTS AND DISCUSSION

The plasma evolved from a laser-irradiated target consists of a steepened region near the critical density and a relatively long scale length plasma below the critical density. The coronal plasma is spatially isothermal up to the steepened region, within which the temperature drops rapidly. Time-integrated measurements of the laser absorption, coronal temperature (from hard x rays), and M-band emission are discussed in Sec. III A. The electron density spatial profiles, which have a strong temporal dependence, are discussed, respectively, in Secs. III B and III C for the high density ($n_c/4 - n_c/2$) and low density ($n_c/200 - n_c/5$) portions of the corona. The laser spot size (Sec. III D) and laser intensity pattern (Sec. III E) are seen to have an impact on the evolution of the lower density portion of the corona.

Several pulse shapes were used in the experiment. Since most of the data were obtained for the square and pickets + square laser pulses, we will limit our discussion to those pulse shapes, primarily for the 200 μm spot size. The t-squared pulse shape data and simulations of all of the pulse shapes are discussed in II.

A. Absorption, temperature, and M-band energy

The absorption percentages $(E_{inc} - E_{ref})/E_{inc} \times 100\%$ are listed in Table II for the various pulse shapes and intensities. The values quoted were obtained by averaging the absorption percentage from at least ten target experiments for each pulse shape. For identical pulse shapes, the laser energy was varied by up to 50%. Since absorption percentage is weakly dependent on intensity, we average our data in two intensity groups, $2\text{–}5\times10^{14}$ W/cm^2 and $0.4\text{–}1\times10^{14}$ W/cm^2. The lower intensities occurred for the larger spot size. The square and pickets + square irradiations had nearly the same absorption percentages, $75 \pm 5\%$ and $90 \pm 3\%$ for the high and low intensities, respectively. The 2 nsec square pulse irradiations had absorption percentages that were from 5% to 10% higher than the 850 psec experiments, consistent with the energy on target remaining constant, but intensity being lower. Our absorption measurements agree well with data taken elsewhere for square and Gaussian shaped laser pulses.[3–15]

TABLE II. Absorption, estimated coronal temperature, and scale length (between $n_c/10$ and $n_c/40$) at the end of the laser pulse are listed for the various pulse shapes and spot sizes.

Pulse shape	Spot size (μm)	Intensity (10^{14} W/cm^2)	Absorption (%)	T_e (keV)	Scale length (μm)
850 psec	200	2–5	78 ± 4	2.4 ± 0.5	100 ± 20
square	500	0.4–1	82 ± 1	1.7 ± 0.4	
2 nsec	200	1–3	82 ± 7	1.7 ± 0.2	120
square	500	0.2–0.5	95 ± 2		120
pickets +	200	2–5	74 ± 4	2.5 ± 0.5	100
square	500	0.4–1	90 ± 2	1.4 ± 0.3	

The measured average coronal temperatures obtained from the x-ray flux were 2.4 ± 0.5 keV for the high intensity ($200\,\mu$m spot) and 1.5 ± 0.2 keV for low intensity ($500\,\mu$m and 2 nsec square pulse) experiments. The data were obtained from averaging temperatures from at least three irradiations with similar intensities for each pulse shape. The temperatures are in good agreement with those obtained from the nonflux limited simulations ($T_e = 2.1$–2.3 keV) for both the high intensity square and pickets + square laser pulse shapes. We did not observe a systematic difference in temperature variation with pulse shape for experiments with similar peak intensities. Hard x-ray emission, as evidenced by M-band emission and code simulations, has a strong dependence on laser intensity. The electron temperature measurement from hard x rays is therefore dominated by the electron temperature during peak laser irradiation. Since the peak laser intensities are similar for the square and pickets + square pulse shapes, we expect the measured electron temperatures to be similar. The experimentally determined temperatures can be readily compared to a scaling law obtained from earlier LASNEX simulations[6] for similar irradiation parameters, namely, $T_e = 2.3 I_{14}{}^{0.45} \lambda_\mu{}^{0.85}$ keV, where I_{14} is the laser intensity in units of 10^{14} W/cm^2 and λ_μ is the laser wavelength in microns. From this we obtain $T_e = 1$–1.3 keV for the low intensity and $T_e = 1.8$–2.8 keV for the high intensity irradiations.

The measured M-band emission was 3%–5% of the incident laser energy, also in agreement with the measurements of other experiments.[9]

B. Peak M-band emission trajectory

The x-ray streak images can be used to study the motion of the peak M-band emission which we assume (based on simulations and consistent with $3/2\omega$ emission) comes from the region between $n_c/4$ and $n_c/2$. We will discuss the peak M-band emission trajectory for square and pickets + square laser pulses. The peak emission never occurred more than $100\,\mu$m from the target surface, which is much smaller than either the 200 or $500\,\mu$m spot sizes used in the experiment. Therefore, we expect that the effect of geometric divergence is negligible, and differences in the trajectory are due to the laser pulse shape or the intensity. Our simulations were in good agreement with the measurements.

Figure 5(a) shows typical data for the motion of this emission for the nominal 850 psec square laser pulse shapes for high intensity irradiations ($I = 3$–5×10^{14} W/cm^2) with a $200\,\mu$m spot size. The peak emission region moves out to a maximum distance of 45–60 μm from the original target surface by the end of the laser pulse. The peak emission trajectory is linear and has a velocity from 5–7×10^6 cm/sec, increasing with average laser intensity. The nominal 2 nsec square pulse experiments with both a 200 and $500\,\mu$m spot also show linear peak emission trajectories, with only slightly slower velocities of 4–5×10^6 cm/sec. The intensities for these experiments were from 0.5–3×10^{14} W/cm^2. The peak emission regions moved out to a maximum distance of 80–100 μm. The weak dependence of this velocity on intensity makes sense from simple scaling law arguments. We expect the profile velocity near critical density to vary like sound speed C_s. Because $C_s \propto T_e{}^{1/2}$ and, near critical density, $T_e \propto I^{2/3}$, we expect the profile velocity to vary like $I^{1/3}$ in good agreement with the measurements.

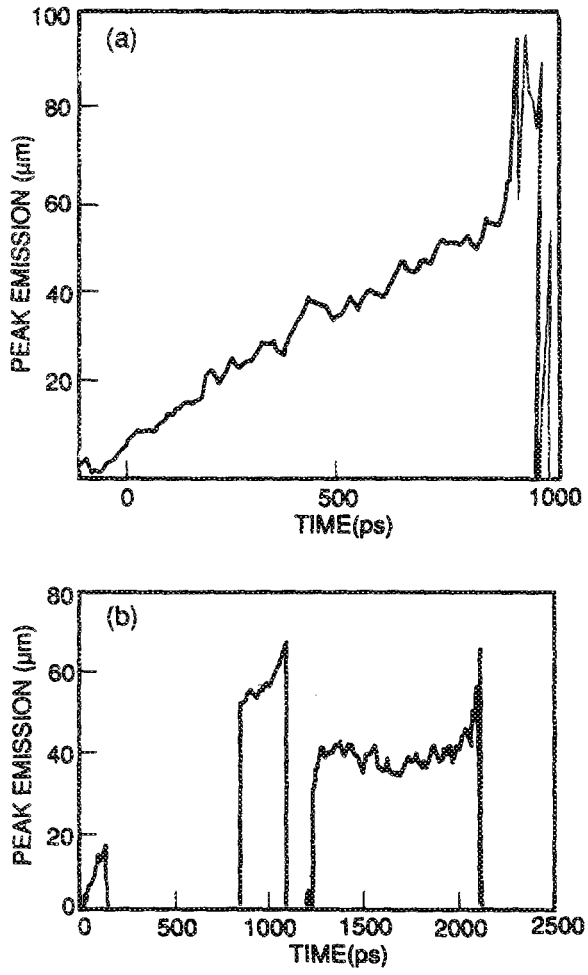

FIG. 5. The peak emission of the M-band x rays along the laser axis occur from near critical density. Square pulses (a) have a linear trajectory and the pickets + square pulses (b) show a retrograde motion (i.e., emission moves toward the target) during the square pulse portion.

The high intensity pickets + square pulses had average intensities (during the square pulse portion) comparable to the 850 psec square pulses discussed above. For the pickets + square pulses, we observe emission corresponding to each picket, as seen in Fig. 5(b). The emission during the first picket occurs from the target surface out to about 20 μm. During the delay between the first and second pickets, the expansion continues, but the emission stops because the plasma has cooled by radiation emission and expansion. The second picket shows a peak emission 40–55 μm from the target surface, yielding a peak emission velocity of 3–4×10^6 cm/sec during the period of expansion while the laser is off. Orthogonal time integrated pinhole photographs of the M-band emission show a gap in the emission region corresponding to the time interval between the first and second pickets. The distance between the emission peaks gives a velocity in agreement with that obtained from the streak camera data. The square portion of the pulse reaches peak intensity about 340 psec after the peak of the second picket. The emission

from this square pulse starts 10–20 μm closer to the target than that from the second picket. It appears to move slightly toward the target during the middle of the pulse and then slowly away. This is also observed in the simulations for the n_c, $n_c/2$, and $n_c/4$ surfaces. This "retrograde" motion may be due to renewed steepening after relaxation of the density profile while the laser is off between the pickets.

Low intensity pickets + square (500 μm spot, $I = 0.5$–1×10^{14} W/cm^2) pulse irradiations did not exhibit the retrograde motion. The emission during the second picket and the square pulse portion occurred slightly farther from the target compared to the higher intensity irradiations, 60–65 μm.

C. Coronal electron density

The scale length $[L = n_e(dn_e/dx)^{-1}]$ of the coronal electron density profile at low density is important because the threshold of parametric instabilities decreases as scale length increases. We therefore discuss the scale length and its temporal dependence for the various pulse shapes, as well as the evolution of the electron density profile. Detailed simulations of the coronal electron density are discussed in II. In general, the scale lengths obtained from the simulations agreed with the measured scale lengths, but the magnitudes of the profiles exhibited large discrepancies.

The plasma density profiles along the laser axis for typical 850 psec ($I = 3$–4×10^{14} W/cm^2) and 2 nsec ($I = 1$–1.5×10^{14} W/cm^2) square pulse experiments with 200 μm laser spots are shown in Figs. 6(a) and 6(b), respectively. Two separate basis function sets were used in the inversion process, and we take the scatter to be the uncertainty in the measurement. Note that at low density the data lie approximately on a straight line, indicating a nearly exponential profile in this portion of the corona. As we discuss in detail in II, however, the data do not agree with an isothermal rarefaction model. Using the measured scale lengths the isothermal rarefaction model yields $T_e < 1$ keV, much lower than that estimated from the x-ray measurements or calculated in our simulations. Upon comparison, the density profiles are quite similar for the two pulse lengths up to 850 psec. From the figures, we see that the density profile relaxes significantly by 1050 psec for the shorter pulse because the laser is off. The very low density plasma at this time, say 2×10^{19}/cm^3, extends out to about 650 μm, compared to 470 μm for the longer pulse.

It is instructive to consider the trajectories of the 4×10^{20}/cm^3 ($n_c/10$) and 1×10^{20}/cm^3 ($n_c/40$) densities, as shown in Fig. 7(a). The data plotted were obtained from several target irradiations with similar intensities. In those cases where the electron density data not quite extend up to $n_c/10$, the $n_c/10$ location was extrapolated logarithmically. The trajectories for the two pulse shapes are nearly the same during the first 850 psec of the irradiation. The $n_c/10$ surface moves out to 90–120 μm by 600 psec and for the 2 nsec pulses, remains stationary for the duration of the laser pulse. The $n_c/40$ surface moves out to 220–240 μm by 800 psec and thereafter remains nearly stationary. The scale lengths are shown in Fig. 7(b). For the 850 psec pulses, the scale length is about 100 μm by the end of the pulse. The scale length

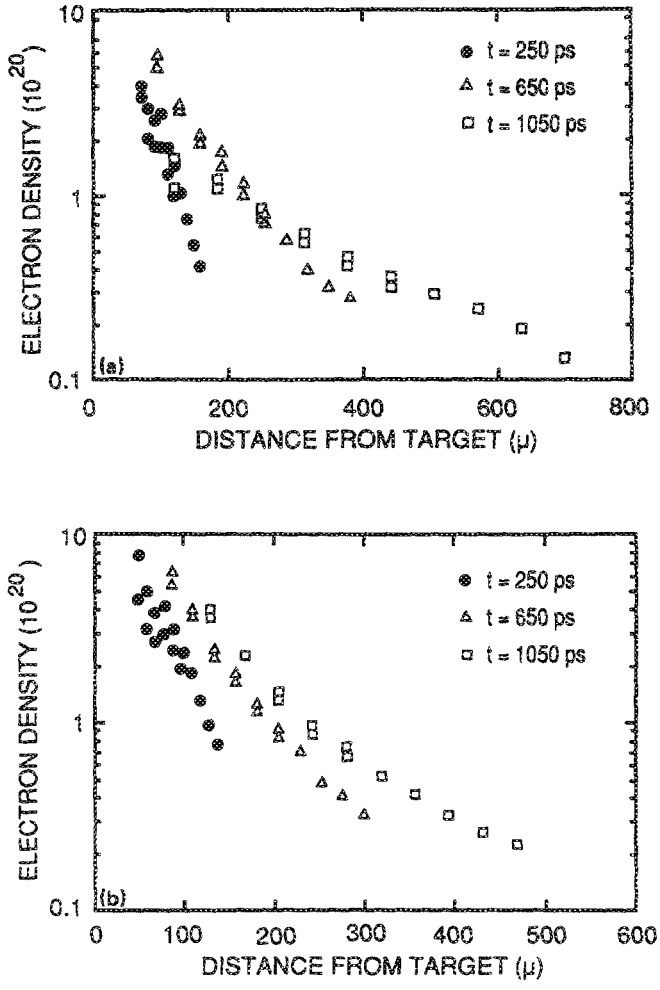

FIG. 6. Plasma density profiles obtained from Abel inversion of interferograms show the plasma expansion for a 850 psec (a) and 2 nsec (b) square pulse irradiation.

reaches about 120 μm by 1 nsec for the 2 nsec irradiations, and remains constant to the end of the laser pulse. As discussed earlier, for some experiments, interferograms were obtained after the laser shut off. In these cases, the scale length increases dramatically (to about 200 μm) within 200 psec after the laser pulse ends.

The scale length temporal dependence is shown in Fig. 7(b) for large spot size (500 μm) but lower intensity ($I = 0.3 \times 10^{14}$ W/cm^2) 2 nsec square pulse irradiations. We see that the scale lengths are slightly less than those for the higher intensity experiments. The scale length increases linearly for about 1 nsec and then remains at 120–140 μm. The $n_c/40$ and $n_c/10$ trajectories are shown in Fig. 8. We observe that the plasma at a given density moves farther from the target at a given time compared to the smaller spot size data shown in Fig. 7(a). The $n_c/40$ and $n_c/10$ velocities are, respectively, 2.4×10^7 and 2.0×10^7 cm/sec.

The square pulse scale lengths can be compared to a scaling law obtained from previous LASNEX simulations[6] (1 ns square laser pulse, 450 μm spot) for the plasma density scale lengths at $n_c/10$, namely, $L_\mu = 114 I_{14}^{0.228} \lambda_\mu^{0.09}$. This shows a rather weak dependence on intensity which we also see in comparing the 2 nsec experiments to the 850 psec

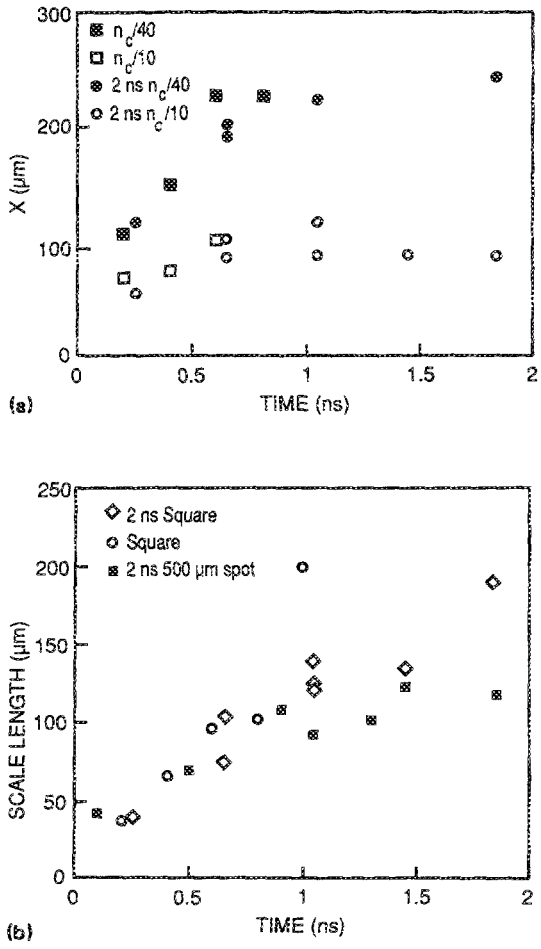

FIG. 7. The trajectories of the $n_c/10$ and $n_c/40$ surfaces (a) for the square pulse irradiation reach a steady state late during the laser pulse. The scale lengths (b) in the low density corona (between $n_c/40$ and $n_c/10$) are constant late in time, 100–200 μm.

experiments at or near 850 psec. The measured scale lengths for this experiment at times near 1 nsec were from 90–140 μm. This compares quite well to the scaling law, which yields $L = 90$–$150\ \mu$m.

We now move on to a discussion of the pickets + square pulse shapes. The interferograms show two interesting features. First, between the first and second pickets, long scale spikes are observed. These spikes, corresponding to plasma jets, will be discussed in more detail in Sec. III E. Since they appear to be localized, and we require cylindrical symmetry for Abel inversion, we do not include the spikes in the digitization of the interferograms. Second, we have observed a rippling of the fringes after the laser is shut off. (This is true for all of the pulse shapes.) The rippling appears everywhere in the expansion from 0.5 to 1 ns after the laser has shut off. It is not as pronounced as the plasma jet, and for inversion of the data between the picket pulses we least-squares smooth the ripples. This smoothing allows us to invert (using an Abel transform) the interferograms to obtain bulk plasma density profiles. The rippling, and the opacity of the cold gold plasma to the probe after the laser is shut off, limited the probing of the square pulses to no more than 500 psec after the laser pulse.

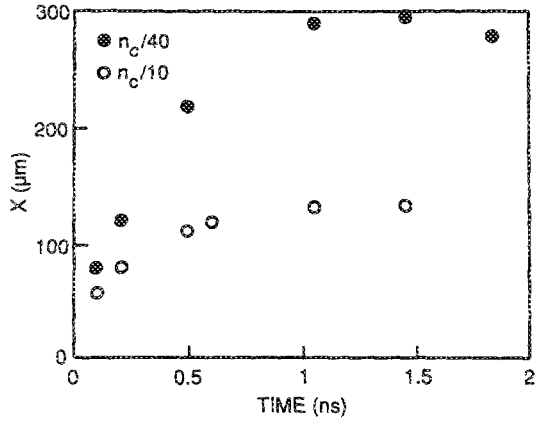

FIG. 8. The trajectory of the $n_c/10$ surface for the 500 μm spot size with 2 nsec square pulse irradiation is similar to that obtained for the smaller spot size. The $n_c/40$ surface, however, moves out farther before reaching a steady state.

Figure 9 shows a typical on-axis plasma density profile for a pickets + square laser pulse with a 200 μm spot size with peak intensity of about 3×10^{14} W/cm^2 for the square pulse portion. Because of the discrete nature of the laser drive, the density profiles are at no time fit well by an exponential profile, in concurrence with the simulations.

The $n_c/10$ and $n_c/40$ surface trajectories for three similar (200 μm spot, $I = 3\times10^{14}$ W/cm^2) irradiations are shown in Fig. 10(a). The shaded region on the abscissa indicates when the laser was on. Our simulations predict that the $n_c/10$ surface should move toward the original target surface between the first and second pickets, as well as between the second picket and square part of the pulse. In the experiment, we observe that between the first and second picket, the trajectory of the $n_c/10$ surface is nonlinear, in contrast to the $n_c/10$ trajectory for the square pulse shown in Fig. 7(a). Upon comparison to the 2 nsec square pulse data, we find that the surfaces move out to about the same distances by the end of the pulse. As expected, the initial trajectories for the pickets + square pulses are slower since the irradiation intensity is lower during the first nanosecond.

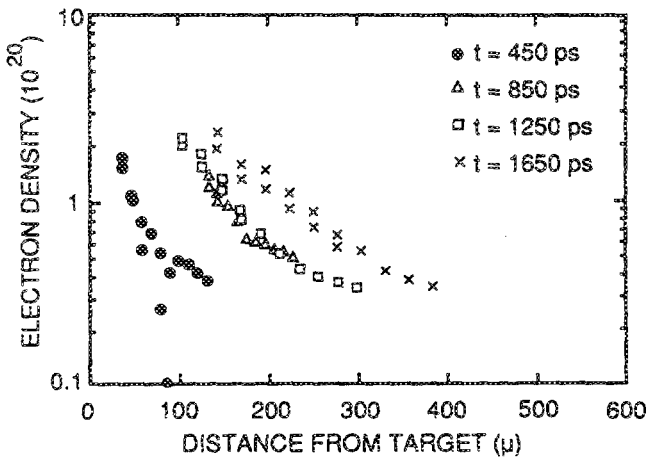

FIG. 9. Density profiles for a typical pickets + square laser pulse irradiation ($I \simeq 3\times10^{14}$ W/cm^2, spot size 200 μm) are not fit well by an exponential.

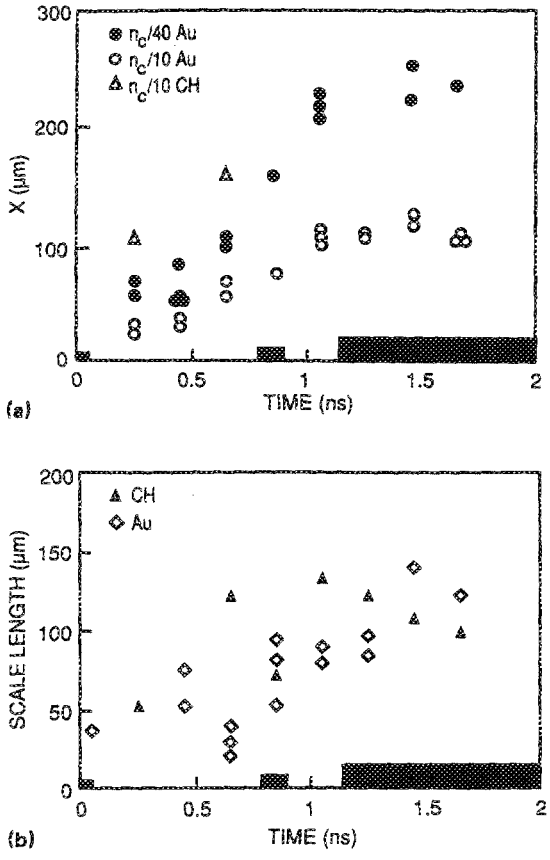

FIG. 10. The trajectories of the $n_c/10$ and $n_c/40$ surfaces (a) for pickets + square pulse irradiation show a discontinuous motion between the pickets, also seen in the simulations. The scale lengths (b) in the low density corona are not well defined during the picket phase, but reach values similar to those for square pulse irradiations at late times. The shaded region on the abscissas indicates when the laser is on.

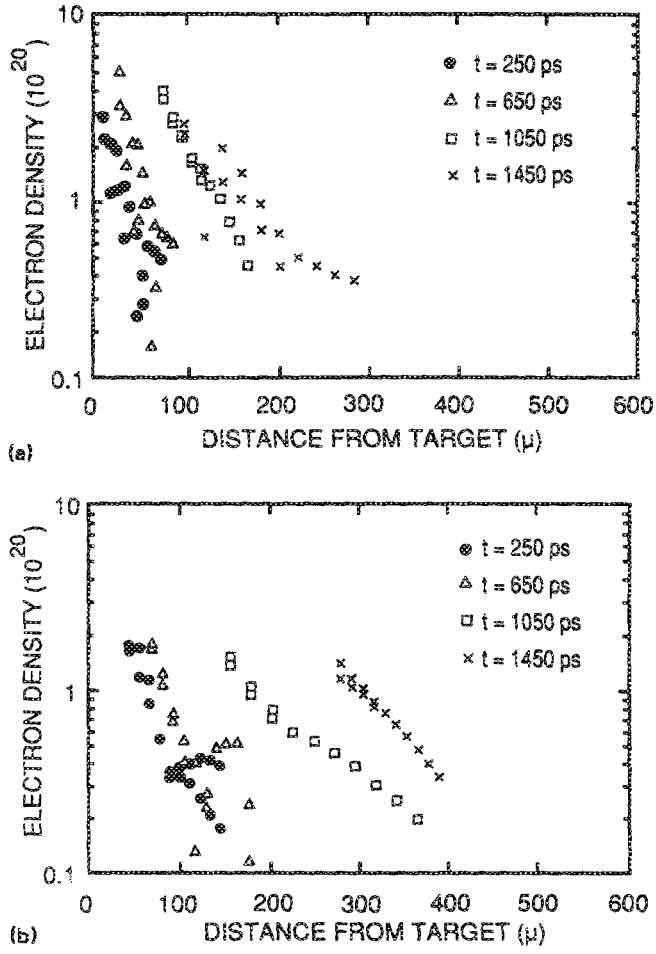

FIG. 11. The effects of laser spot size are shown for two experiments with similar intensities. (a) and (b) show the on-axis density profiles for the 200 and 500 μm spot sizes at $I \simeq 1 \times 10^{14}$ W/cm^2. Note that the plasma expands farther for a given density at a given time for the larger spot size.

The evolution of the scale lengths is shown in Fig. 10(b). In this case, the scale length was calculated by fitting the data to an exponential only between $n_c/10$ and $n_c/40$, since inclusion of the lower density data did not provide as good a fit. Early in the irradiation we see that the scale lengths are less than 50 μm. During the square portion of the pulse the scale length flattens out to about 100 μm, the same as for the square pulse irradiations. Shown also in Figs. 10(a) and 10(b) are data for plastic (CH) targets. We note that the CH trajectories are faster, and the scale length is greater, as expected because the sound speed is higher for CH as compared to gold.

D. Spot size effects

Geometric divergence affects the plasma profiles at distances greater than the spot size.[20,21] Here, we discuss the effect of spot size on the low density coronal expansion by comparison of the M-band emission and electron density profiles for 200 and 500 μm spot size irradiations. The pulse shape was the pickets + square with similar intensities ($I = 1 \times 10^{14}$ W/cm^2) for the two spot sizes.

As stated in Sec. III B, we do not observe geometric divergence to play a role in the peak M-band emission trajectory for the different spot sizes. Pinhole pictures and streaks of the peak emission do not show significant differences in the trajectory of the peak emission surface. Since peak M-band emission comes from near $n_c/2$, which is less than 70 μm from the original target surface, the motion is expected to be similar for both large and small spot sizes.

Interferograms were taken at identical times for the experiments being compared. The plasma densities are shown in Figs. 11(a) and 11(b) for the 200 and 500 μm spot sizes, respectively. At early times (250 and 650 psec) there is good agreement between the measured densities. (We note that for smaller spot sizes, targets can be probed to higher densities since the path lengths through the plasma are smaller.) At late times (1050 and 1450 psec) we find that a given plasma density, say 1×10^{20}/cm^3, is farther from the target surface for the larger spot size. For the 200 μm spot these distances are 150 and 200 μm and for the 500 μm spot, the distances are 180 and 300 μm. We expect the plasma flow to be planar at early times, then later become three-dimensional after the plasma has expanded to distances from the target that are greater than or equal to (roughly) the laser spot size. The transition to three-dimensional expansion therefore occurs later for the larger spot size; the transition is discussed further in II. Additionally, we note that two-dimensional reconstructions of the electron density show greater curvature of the isodensity contours for the smaller spot size.

E. Laser intensity pattern effects

Holographic interferograms of the square pulse experiments show smooth expanding sets of fringes, while the pickets + square pulse irradiations show sharp fringes of up to 300 μm length and width from 20 to 100 μm that are present between the first and second pickets. These jets of plasma smooth during the square portion of the picket pulse. Figures 12(a) and 12(b) shows the evolution of such jets for a two picket pulse with a 200 μm spot size. The peak intensity is about 1×10^{14} W/cm^2. Inversion of the outermost fringe assuming a parabolic profile for the second holographic frame gives a density of 5×10^{20}/cm^3. The tip of this jet has a velocity of about 5×10^7 cm/sec. Similar jets occurred for the 500 μm spot size irradiations.

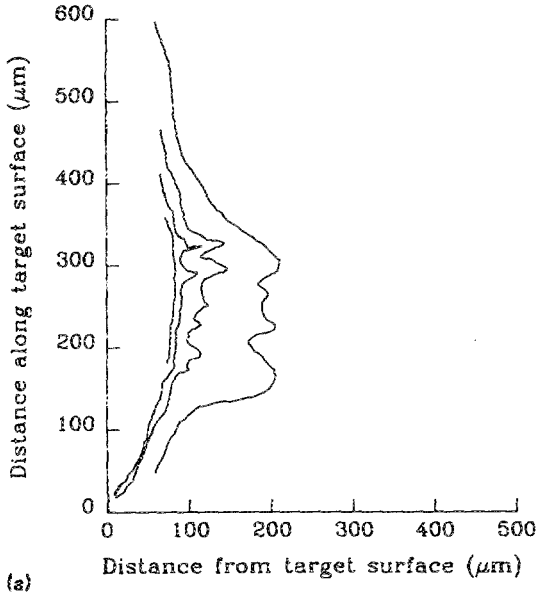

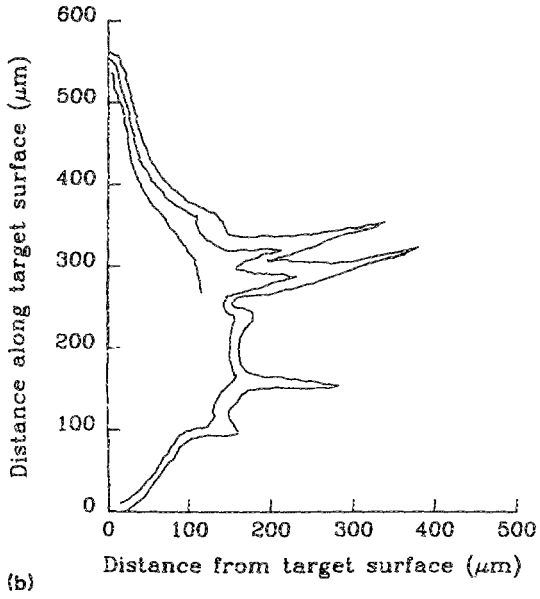

FIG. 12. Digitized interferograms are shown for a two picket laser pulse irradiation with a peak intensity $I\simeq1\times10^{14}$ W/cm^2 and a 200 μm spot. Between the pickets (a) and (b) spikes are seen in the fringe pattern. These plasma jets are smoothed by the laser during the square portion of the pickets + square pulse.

We also observe features in the soft and hard x-ray emission that correspond to these jets. Figure 13 shows the soft and hard emission for a two picket experiment with a 500 μm spot and a peak intensity of 0.8×10^{14} W/cm^2. The soft x-ray emission [Fig. 13(a)] shows high intensity spikes whereas the hard x-ray emission [Fig. 13(b)] shows a lower emission in roughly the same place. This is evidence that the plasma jets are cooler and denser than the neighboring coronal plasma. The jets appeared in the time integrated images only for the two picket irradiations. For the pickets + square pulse shapes, the jets were visible only in the interferograms, which provide time resolution. We hypothesize that the square portion of the laser pulse pumps enough energy into the expanding jets that they equilibrate with the rest of the coronal plasma, and so are not discernable in the time integrated images. The jets were observed for both small (high intensity) and large (low intensity) spot size irradiations.

Separate experiments[22] with the target placed on the convergent side of best focus [that is, with a hot ring intensity pattern, as in Fig. 2(b)] show that these jets arise from the cold spots. Two-dimensional hydrocode modeling has not been successful in replicating this phenomenon, implying that simple hydrodynamics is not the case. The details of the modeling efforts on these plasma jets are reported elsewhere.[23]

IV. SUMMARY

We have irradiated gold disk targets with intensities and pulse shapes of interest to laser fusion. The temperatures and laser absorptions are in good agreement with previous experiments and our simulations. Measurements of the high density $n_c/2$–$n_c/4$ trajectory behave as expected, showing a weak dependence on laser intensity. For pickets + square

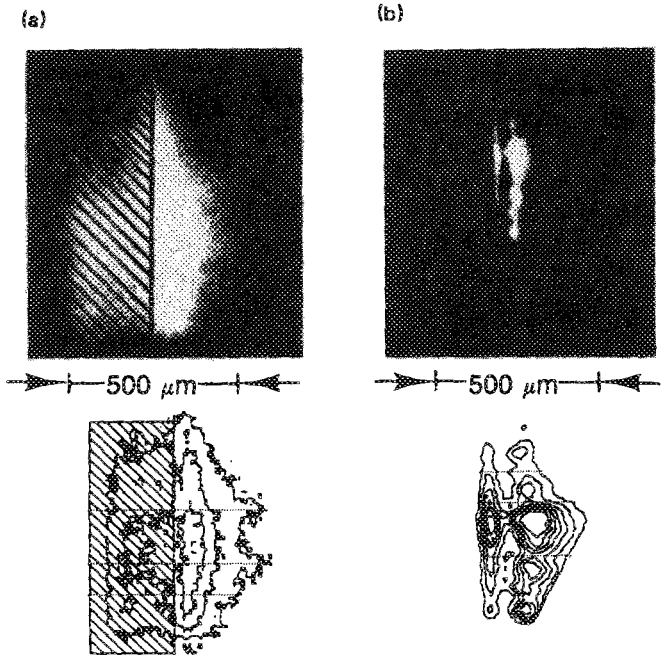

FIG. 13. X-ray images for a two picket pulse show that the plasma jets are cold and dense. The jets emit soft x-rays (a) and absorb M-band x rays (b).

laser pulses we have observed a retrograde motion of this region, also predicted by simulations. The low density ($n_c/40$–$n_c/10$) portion of the corona was also measured. The scale lengths are in good agreement with a scaling law for square pulses and with our simulations for square and pickets + square pulse shapes. There is disagreement, however, with the magnitudes of the profiles obtained from the simulations. In addition, we have observed plasma jetting from cold spots in the laser intensity pattern, which have not to date been replicated in our two-dimensional simulations. Further aspects of the jetting are discussed in a separate paper.[22] Detailed simulations of the experiments discussed here are described in an accompanying paper.[1]

ACKNOWLEDGMENTS

We thank Dr. Linda Powers and Dr. Dick Berger for useful discussions. Technical support for these experiments was provided by David Sullivan and John Brundage. Film scans were done by Alma Williams. The Kirkpatrick–Baez microscope, along with assistance on its operation, was provided by Bill Cook of Lawrence Livermore National Laboratory.

This work was prepared for the U.S. Department of Energy under Contract No. DE-AC03-87DP10560.

[1] D. Ress, L. Suter, E. F. Gabl, and B. H. Failor, Phys. Fluids B **2**, 2448 (1990).
[2] G. B. Zimmerman and W. L. Kruer, Comments Plasma Phys. Controlled Fusion **11**, 51 (1975).
[3] K. Tanaka, L. M. Goldman, W. Seka, M. C. Richardson, J. M. Soures, and E. A. Williams, Phys. Rev. Lett. **48**, 1179 (1982).
[4] W. Seka, E. A. Williams, R. S. Craxton, L. M. Goldman, R. W. Short, and K. Tanaka, Phys. Fluids **27**, 2181 (1984).
[5] C. L. Shepard, J. A. Tarvin, R. L. Berger, Gar. E. Busch, R. R. Johnson, and R. J. Schroeder, Phys. Fluids **29**, 583 (1986).
[6] R. E. Turner, K. G. Estabrook, R. L. Kauffman, D. R. Bach, R. P. Drake, D. W. Phillion, B. F. Lasinski, E. M. Campbell, W. L. Kruer, and E. A. Williams, Phys. Rev. Lett. **57**, 1725 (1985).
[7] R. P. Drake, Phys. Fluids B **1**, 1082 (1989) and references therein.
[8] M. D. Rosen, D. W. Phillion, V. C. Rupert, W. C. Mead, W. L. Kruer, J. J. Thomson, H. N. Kornblum, V. W. Slivinsky, G. J. Caporaso, M. J. Boyle, and K. G. Tirsell, Phys. Fluids **22**, 2020 (1979).
[9] W. C. Mead, E. M. Campbell, K. G. Estabrook, R. E. Turner, W. L. Kruer, P. H. Y. Lee, B. Pruett, V. C. Rupert, K. G. Tirsell, G. L. Stradling, F. Ze, C. E. Max, and M. D. Rosen, Phys. Rev. Lett. **47**, 1289 (1981); W. C. Mead, E. M. Campbell, K. G. Estabrook, R. E. Turner, W. L. Kruer, P. H. Y. Lee, B. Pruett, V. C. Rupert, K. G. Tirsell, G. L. Stradling, F. Ze, C. E. Max, M. D. Rosen, and B. F. Lasinski, Phys. Fluids **26**, 2316 (1983).
[10] H. Nishimura, F. Matsuoka, M. Yagi, Y. Yamada, S. Nakai, G. H. McCall, and C. Yamanaka, Phys. Fluids **26**, 1688 (1983).
[11] W. C. Mead, S. V. Coggeshall, S. R. Goldman, E. K. Stover, P. D. Goldstone, J. Cobble, A. Hauer, G. Stradling, J. M. Kindel, L. Montierth, M. C. Richardson, O. Barnouin, P. Jaanimagi, F. Marshall, R. Marjoribanks, R. L. Kauffman, H. N. Kornblum, and B. F. Lasinski, in *Laser Interaction and Related Plasma Phenomena*, edited by H. Hora and G. H. Miley (Plenum, New York, 1986), Vol. 7, p. 723.
[12] R. Kodama, K. Okada, N. Ikeda, M. Mineo, K. A. Tanaka, T. Mochizuki, and C. Yamanaka, J. Appl. Phys. **59**, 3050 (1986).
[13] P. D. Goldstone, S. R. Goldman, W. C. Mead, J. A. Cobbie, R. H. Day, A. Hauer, M. C. Richardson, R. S. Marjoribanks, P. A. Jaanimagi, R. L. Keck, F. J. Marshall, W. Seka, O. Barnouin, B. Yaakobi, and S.A. Letzring, Phys. Rev. Lett. **59**, 56 (1987).
[14] F. Ze, D. R. Kania, S. H. Langer, H. Kornblum, R. Kaufman, J. Kilkenny, E. M. Campbell, and G. Tietbohl, J. Appl. Phys. **66**, 1935 (1989).
[15] J. Delletrez, Can. J. Phys. **64**, 432 (1986) and references contained therein.
[16] E. M. Campbell, J. T. Hunt, E. S. Bliss, D. R. Speck, and R. P. Drake, Rev. Sci. Instrum. **57**, 2101 (1986).
[17] C. E. Thomas and L. D. Siebert, Appl. Opt. **15**, 462 (1976).
[18] F. Seward, J. Dent, M. Boyle, L. Koppel, T. Harper, P. Stoering, and A. Toor, Rev. Sci. Instrum. **47**, 464 (1976).
[19] G. E. Busch, C. L. Shepard, L. D. Siebert, and J. A. Tarvin, Rev. Sci. Instrum. **56**, 879 (1985).
[20] C. E. Max, C. F. McKee, and W. C. Mead, Phys. Fluids **23**, 1620 (1980).
[21] S. Gitomer, R. Morse, and B. Newberger, Phys. Fluids **20**, 234 (1977).
[22] E. F. Gabl, B. H. Failor, C. J. Armentrout, R. A. Bosch, Gar. E. Busch, N. D. Delamater, W. B. Fechner, Z. Koenig, D. Ress, L. Suter, and R. J. Schroeder, Phys. Rev. Lett. **63**, 2737 (1989).
[23] W. B. Fechner and N. D. Delamater, Bull. Am. Phys. Soc. **34**, 2023 (1989).